Low-Dose NIR-II Preclinical Bioimaging Using Liposome-Encapsulated Cyanine Dyes

Duyang Gao, Zichao Luo, Yang He, Lixiang Yang, Dehong Hu, Yongye Liang, Hairong Zheng,* Xiaogang Liu,* and Zonghai Sheng*

Fluorescence imaging in the second near-infrared window (NIR-II, 1000–1700 nm) provides a powerful tool for in vivo structural and functional imaging in deep tissue. However, the lack of biocompatible contrast agents with bright NIR-II emission has hindered its application in fundamental research and clinical trials. Herein, a liposome encapsulation strategy for generating ultrabright liposome-cyanine dyes by restricting dyes in the hydrophobic pockets of lipids and inhibiting the aggregation, as corroborated by computational modeling, is reported. Compared with free indocyanine green (ICG, an US Food and Drug Administration-approved cyanine dye), liposome-encapsulated ICG (S-Lipo-ICG) shows a 38.7-fold increase in NIR-II brightness and enables cerebrovascular imaging at only one-tenth dose over a long period (30 min). By adjusting the excitation wavelength, two liposome-encapsulated cyanine dyes (S-Lipo-ICG and S-Lipo-FD1080) enable NIR-II dual-color imaging. Moreover, small tumor nodules (2–5 mm) can be successfully distinguished and removed with S-Lipo-ICG image-guided tumor surgery in rabbit models. This liposome encapsulation maintains the metabolic pathway of ICG, promising for clinical implementation.

1. Introduction

Fluorescence imaging in the second near-infrared window (NIR-II, 1000–1700 nm) has become an important tool in fundamental research and clinical practice for real-time, noninvasive optical imaging.[1] This is because it enables the structural and functional imaging in living systems with high resolution and high contrast by suppressing background absorption and photon scattering.[2] Compared with traditional optical imaging, NIR-II fluorescence imaging has been widely applied in the monitoring of brain diseases,[3] tracking of immune cells,[4] measuring blood flow velocity,[5] and other fields.[6] Additionally,

compared with the first near-infrared window (NIR-I, 650–950 nm)-based imaging, NIR-II fluorescence imaging has been used to navigate human liver cancer surgery under bright-field conditions.[1d] However, NIR-II fluorescence imaging is severely limited by the low brightness of the contrast agents. For the clinical translation of NIR-II fluorescence imaging, it is essential to explore contrast agents with bright NIR-II emission.

To date, various types of NIR-II contrast agents have been constructed and employed in different disease fields.[7] Among them, low molecular weight cyanine dyes are of great importance owing to the successful clinical application of indocyanine green (ICG), a cyanine dye approved by the US Food and Drug Administration (FDA) for NIR-II fluorescence imaging.[1d,8] Recent studies have focused on molecular engineering strategies or advanced nanotechnology to enhance the imaging performance of cyanine dyes (e.g., emission wavelength, stability, and circulation time) and to expand their phototheranostic applications.[9] However, despite the considerable progress, it remains a major challenge to improve the brightness of ICG's NIR-II emission in vivo, which is affected by the excitation absorption coefficient and fluorescence quantum yield (QY).

Herein, we report a general strategy to simultaneously enhance the absorption coefficient of cyanine dyes (ICG, IR780 and FD1080) and their NIR-II fluorescence QY for preclinical bioimaging. Low-concentration cyanine dyes are encapsulated in liposomes, a type of clinically used drug delivery system. This results in an emission wavelength redshift and absorption

D. Gao, D. Hu, H. Zheng, Z. Sheng
Paul C. Lauterbur Research Center for Biomedical Imaging
CAS Key Laboratory of Health Informatics
Shenzhen Key Laboratory of Ultrasound Imaging and Therapy
Institute of Biomedical and Health Engineering
Shenzhen Institute of Advanced Technology
Chinese Academy of Sciences
Shenzhen 518055, P. R. China
E-mail: hr.zheng@siat.ac.cn; zh.sheng@siat.ac.cn

The ORCID identification number(s) for the author(s) of this article can be found under https://doi.org/10.1002/smll.202206544.

Z. Luo, X. Liu
Department of Chemistry and Center for NanoMedicine
National University of Singapore
Singapore 117543, Singapore
E-mail: chmlx@nus.edu.sg
Y. He, L. Yang
BayRay Innovation Center
Shenzhen Bay Laboratory
Shenzhen 518055, P. R. China
Y. Liang
Department of Materials Science and Engineering
Southern University of Science and Technology
Shenzhen 518055, P. R. China

2206544 (1 of 12)

enhancement. The NIR-II fluorescence brightness of liposome-ICG (S-Lipo-ICG) is 38.7-fold higher than that of free ICG, enabling low-dose cerebrovascular imaging (0.04 mg kg^{-1}). Moreover, we report for the first time excitation-dependent dual-color NIR-II imaging using two different S-Lipo-cyanine dyes, providing a new toolbox for monitoring complex biological processes. Furthermore, the scaleup of S-Lipo-ICG enables imaging-guided tumor surgery in rabbit models. The liposome encapsulation of ICG improves NIR-II fluorescence imaging but maintains the metabolic pathway, which is promising for clinical translation.

2. Results and Discussion

2.1. Liposome Encapsulation Strategy

As displayed in **Figure 1**A, our strategy involved the encapsulation of cyanine dyes into the lipids through hydrophobic

interactions for generating ultrabright liposome-cyanine dyes (S-Lipo-Cyanine dye). Hence, we first mixed the cyanine dyes with lipids (1,2-distearoyl-sn-glycero-3-phosphoethanolamine-N-[methoxy(polyethylene glycol)-2000]) (DSPE-PEG$_{2000}$) and 1,2-dioleoyl-sn-glycero-3-phosphocholine (DOPC)) in an organic solvent, since it can prevent the potential aggregation of dyes commonly observed in aqueous solutions. The S-Lipo-Cyanine dye was further obtained via a modified high-pressure homogenization method.[10] Cyanine dyes, including commercial ICG, IR780, and the synthetically prepared FD1080,[11] were used to assess the universality of this strategy. After liposome encapsulation, hazy transparent solutions of S-Lipo-ICG, S-Lipo-IR780, and S-Lipo-FD1080 were obtained, indicating efficient encapsulation of cyanine dyes in liposomes (Figure S1, Supporting Information). The hydrodynamic diameters of S-Lipo-ICG, S-Lipo-IR780, and S-Lipo-FD1080 measured by dynamic light scattering were 119.5, 129.3, and 128.1 nm, respectively, which further confirmed the feasibility of the strategy (Figure S2,
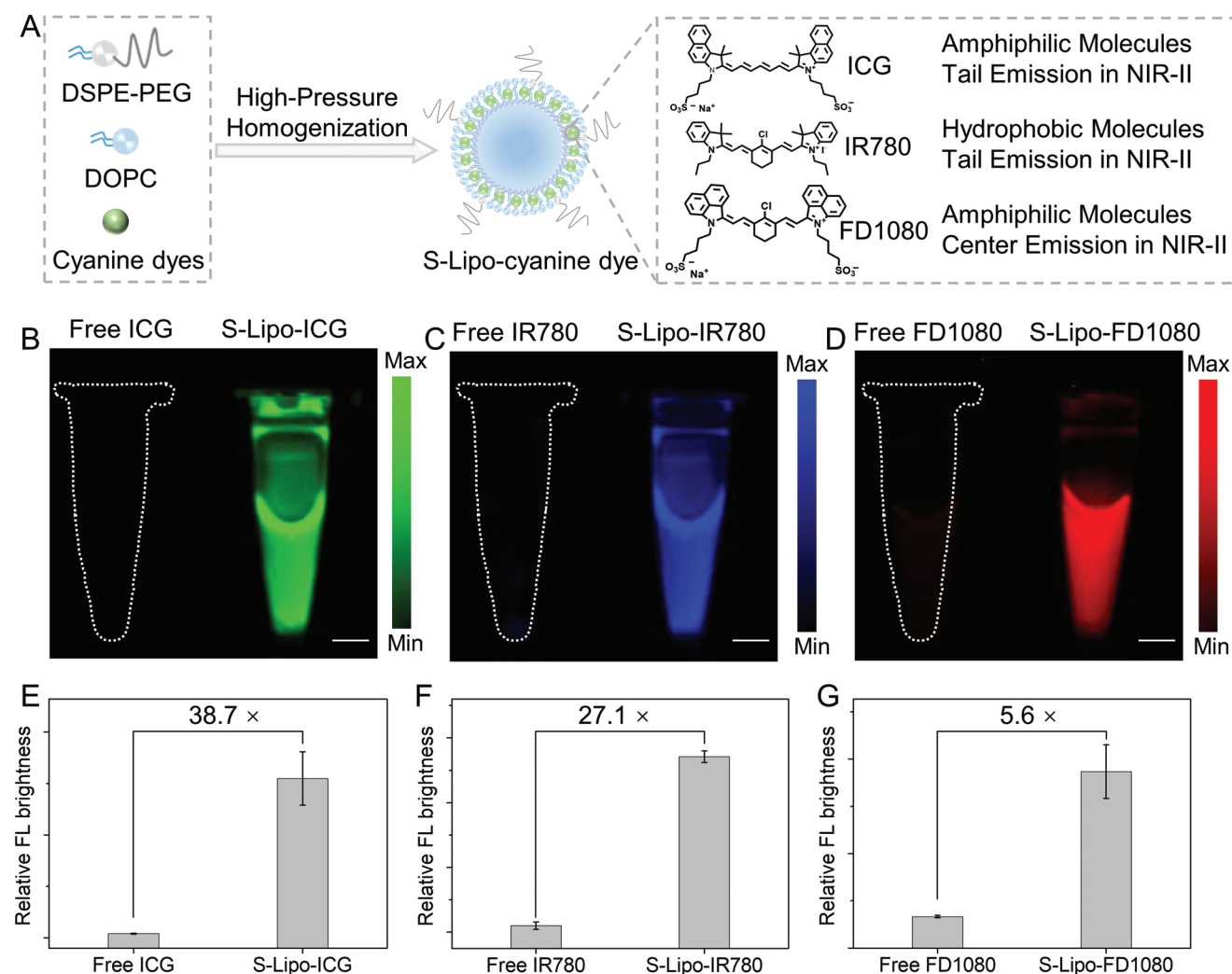

Figure 1. Preparation and characterization of S-Lipo-dye. A) Schematic illustration of the preparation of S-Lipo-ICG, S-Lipo-IR780, and S-Lipo-FD1080 by high-pressure homogenization. B–D) NIR-II fluorescence images of free ICG and S-Lipo-ICG (B), free IR780 and S-Lipo-IR780 (C), free FD1080 and S-Lipo-FD1080 (D), respectively (ICG, green pseudocolor, 2.5 mW cm^{-2}, 808 nm excitation, LP1000, 2 ms; IR780, blue pseudocolor, 2.5 mW cm^{-2}, 808 nm excitation, LP1000, 5 ms; FD1080, red pseudocolor, 2.5 mW cm^{-2}, LP1100, 50 ms). Scale bar: 5 mm. E–G) NIR-II fluorescence brightness comparison between free cyanine dyes and S-Lipo-dye from (B–D), including ICG, IR780, and FD1080, respectively. Mean values are presented and error bars are ± s.d ($n = 5$).

Supporting Information). In addition, liposome encapsulation improved the water-solubility of IR780, thereby improving its applicability in biomedical fields. Subsequently, the NIR-II fluorescence images of the free cyanine dye solution and S-Lipo-cyanine dye solution within the equivalent mass of the dyes were recorded using a NIR-II fluorescence imaging system under excitation at 808 nm (S-Lipo-ICG, S-Lipo-IR780) and 1064 nm (S-Lipo-FD1080), respectively. The NIR-II fluorescence brightness of the S-Lipo-ICG solution was much stronger than that of the free ICG solution under the same conditions (Figure 1B). Interestingly, similar results were found in S-Lipo-IR780 and S-Lipo-FD1080 solutions, demonstrating that this liposome-encapsulation strategy can enhance the NIR-II fluorescence performance of cyanine dyes (Figure 1C,D). Quantitative analysis revealed that the NIR-II fluorescence brightness of ICG, IR780, and FD1080 was enhanced by 38.7-fold, 27.1-fold, and 5.6-fold, respectively, after liposome encapsulation (Figure 1E–G). These results indicate that liposome encapsulation by high-pressure homogenization provides a general method for preparing liposome-cyanine dyes, which not only improves the water-solubility of the dyes but also enhances their NIR-II fluorescence brightness.

2.2. Characterization of S-Lipo-ICG

Next, S-Lipo-ICG was selected as a representative of liposome-cyanine dyes to investigate the mechanism of NIR-II brightness enhancement, because ICG, a well-known FDA-approved dye, is widely used in the clinical applications. Cryo-electron microscope reveals that S-Lipo-ICG has a core–shell structure with an average particle size of 110 nm (105 nm core, 5 nm shell), which is consistent with the dynamic light scattering profile (**Figure 2**A; Figure S2, Supporting Information). The characteristic absorption peaks of S-Lipo-ICG showed a red shift from 780 to 803 nm, and the absorbance intensity increased ≈2.0-fold compared with that of free ICG dissolved in phosphate-buffered saline (PBS) at the same mass concentration (Figure 2B). These two factors lead to a 4.4-fold increase in the extinction coefficient at 808 nm compared with that of free ICG (Figure 2D). Meanwhile, the fluorescence emissions of S-Lipo-ICG showed a red shift by ≈13 nm (Figure S3, Supporting Information), which enhanced the tail emission in the NIR-II region (Figure 2C). Therefore, the NIR-II fluorescence QY of S-Lipo-ICG is ≈10 times stronger than that of free ICG (Figure 2E). The combination of an increase in the extinction coefficient (808 nm) and NIR-II QY enables intense NIR-II fluorescence of S-Lipo-ICG (Figure 2F, inset). Quantitative measurements showed that the NIR-II fluorescence brightness of S-Lipo-ICG is 12-, 21-, and 195-fold higher than that of reported contrast agents with NIR-II emission, including TTB nanoparticles (NPs),[12] TB1 NPs,[13] and TT molecules,[14] all with equivalent mass concentration (Figure 2F). We next examined the interaction between ICG and the lipid layer in liposomes to explore the possible enhancement mechanism. Note that free ICG in an aqueous solution tends to form dimers and polymers with increasing concentration, which decreases its fluorescence QY.[9d,15] The NIR-II QYs of S-Lipo-ICG increased by ≈10-fold when the lipid/ICG ratio increased from 15 to 250 (Figure 2G). However, the

NIR-II QYs remained nearly unchanged when the Lipid/ICG ratio ranged from 250 to 750. These data indicate that an appropriate amount of ICG (Lipid/ICG = 250:1) incorporated into liposomes can effectively inhibit aggregation-induced fluorescence quenching and thus enhance the NIR-II emission brightness. Importantly, after storage at 4 °C in a freezer for 15 days, the NIR-II fluorescence signal of the S-Lipo-ICG solution was maintained at over 80%, whereas it decline to ≈30% in the free ICG solution (Figure 2H). This indicates that the liposome-encapsulated ICG can enhance optical stability by reducing the photooxidation effect.[5b] We also observed that the size of S-Lipo-ICG remained unchanged during the 15-day storage (Figure 2I), indicating good chemical stability.

2.3. Mechanism Underlying the Interaction between ICG and Liposomes

To better understand the potential mechanism underlying the brightness enhancement of ICG after liposome encapsulation, the interactions between ICG and the liposomes were investigated by molecular docking and molecular dynamics. Note that the docking score was used to evaluate the binding sites and poses of ICG in the liposome. Low and negative binding energies indicate a spontaneous and energetically favorable process between the molecule (ICG) and receptor (liposome). The results of molecule docking analysis revealed that ICG could bind to four different sites on the liposome, and the four binding sites were stably maintained during molecular simulation, resulting in a conformational change (Figure S4, Movie S1, and Table S1, Supporting Information). The generated binding sites of ICG exhibited strong hydrophobic interaction with the surrounding cavities of liposomes owing to the presence of hydrophobic rings and hydrophobic chains (**Figure 3**A). Among the four binding sites, site 1 and site 2 had docking scores of −11.54 and −11.25 kcal mol^{-1}, respectively, suggesting that ICG molecules are likely to adopt those conformations in the hydrophobic shell of the liposome. Different from being embedded into the hydrophobic cavities of liposomes, free ICG exhibited a high stacking tendency in water (Figure 3B; Movie S2, Supporting Information). The stacking pose of ICG not only reduces its fluorescence brightness but also inhibits the encapsulation efficiency (Figure S5, Supporting Information). The computational modeling results indicated that adding the ICG dissolved in organic solvents before film formation with liposomes is an effective strategy to enhance the brightness.

2.4. Cerebrovascular NIR-II Fluorescence Imaging

Noninvasive NIR-II cerebrovascular imaging in mouse models was conducted using S-Lipo-ICG or free ICG after evaluation of their cell toxicity in vitro (Figure S6, Supporting Information). After the intravenous (i.v.) administration of S-Lipo-ICG at a dose of 0.2 mg kg^{-1} (a recommended ICG dose for in vivo imaging), the inferior cerebral vein, superior sagittal sinus, and transverse sinus under the scalp, as well as other cortical veins in both cerebral hemispheres, were clearly visible 0.5 min after i.v. injection (**Figure 4**A). By contrast, we could not view

ADVANCED
SCIENCE NEWS
www.advancedsciencenews.com
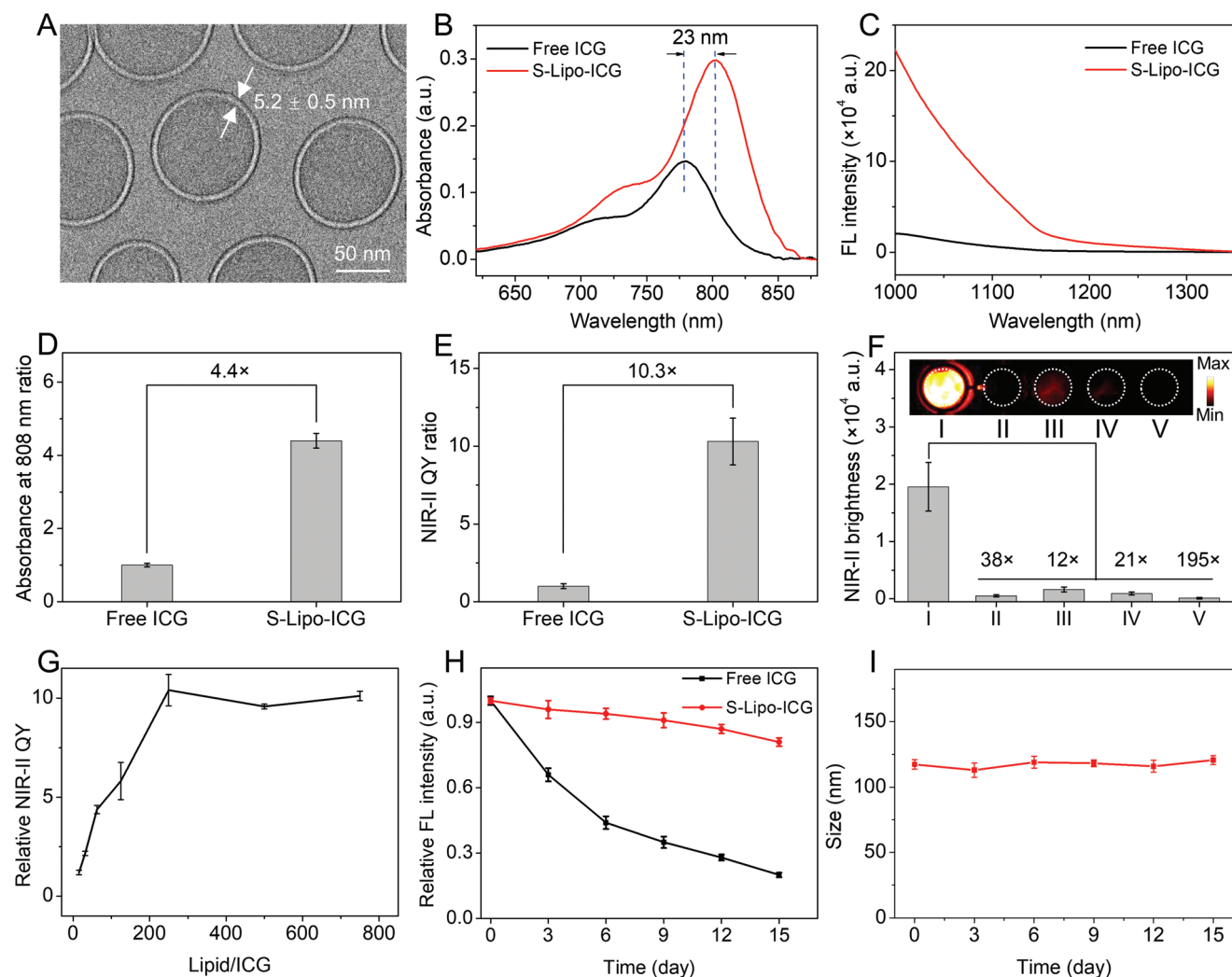
NANO · MICRO
small
www.small-journal.com

Figure 2. Characterization of S-Lipo-ICG and mechanism of brightness enhancement. A) Cryo-electron microscopy image of S-Lipo-ICG. B) Absorption spectra of free ICG and S-Lipo-ICG dispersed in PBS (ICG, 1.25 µg mL^{-1}). C) The NIR-II tail emission of free ICG and S-Lipo-ICG. D) The absorbance (808 nm) comparison of free ICG and S-Lipo-ICG. E) The NIR-II QY comparison of free ICG and S-Lipo-ICG. F) Brightness comparison and NIR-II fluorescence images between S-Lipo-ICG (I), free ICG (II), and other reported NIR-II probes including TTB NPs (III), TB1 NPs (IV), and TT (V) (2.5 mW cm^{-2}, LP1000, 5 ms). G) Effects of different Lipid/ICG ratios on NIR-II QY of S-Lipo-ICG. H) Optical stability of the free ICG and S-Lipo-ICG during 15-day storage. I) Size variation of S-Lipo-ICG during 15-day storage. Means are given and error bars are ± s.d. ($n = 5$).

many cortical arteries in both cerebral hemispheres after the i.v. injection of free ICG at the same dose (0.2 mg kg^{-1}). Of note, dose reduction is beneficial for reducing the likelihood of the adverse effects of ICG. Given the enhanced brightness of S-Lipo-ICG, we performed cerebrovascular imaging at a lower dose of 0.04 mg kg^{-1}. All blood vessels except some cortical arteries could still be visualized in S-Lipo-ICG-treated mice. By contrast, almost no blood vessels were observed in free ICG-treated mice (Figure 4A). The signal-to-background ratio (SBR) at the inferior cerebral vein of S-Lipo-ICG-treated mice were 6 (0.2 mg kg^{-1}) and 4 (0.04 mg kg^{-1}), which were 1.7- and 4-times higher than that of the free ICG-treated mice at the corresponding dose (Figure 4B).

Note that the half-life of an imaging agent in the blood is another key aspect of cerebrovascular imaging.[5b] The pharmacokinetics of free ICG and S-Lipo-ICG were evaluated by

collecting blood samples from mice at different instants after i.v. injection. The NIR-II fluorescence images of blood samples from S-Lipo-ICG-treated mice showed strong fluorescence signals, and could still be detected at 30 min postinjection. By contrast, the NIR-II fluorescence signal from free ICG-treated mice was weak and undetectable 5 min postinjection (Figure 4C). Using a monoexponential decay model, the half-life of free ICG and S-Lipo-ICG in mice was calculated to be 3.0 ± 0.5 min and 16.8 ± 1.7 min, respectively (Figure 4D). This prolongation of the half-life in the blood may aid long-term imaging in vivo. The cerebrovascular system of mice could be observed for up to 30 min (SBR = 1.9) after treatment with S-Lipo-ICG, but these systems could only be visualized within 5 min (SBR = 1.3) in the ICG-treated group (Figure 4E,F). The long-term in vivo imaging potential may be beneficial for imaging-guided tumor surgery, as the optimal surgical
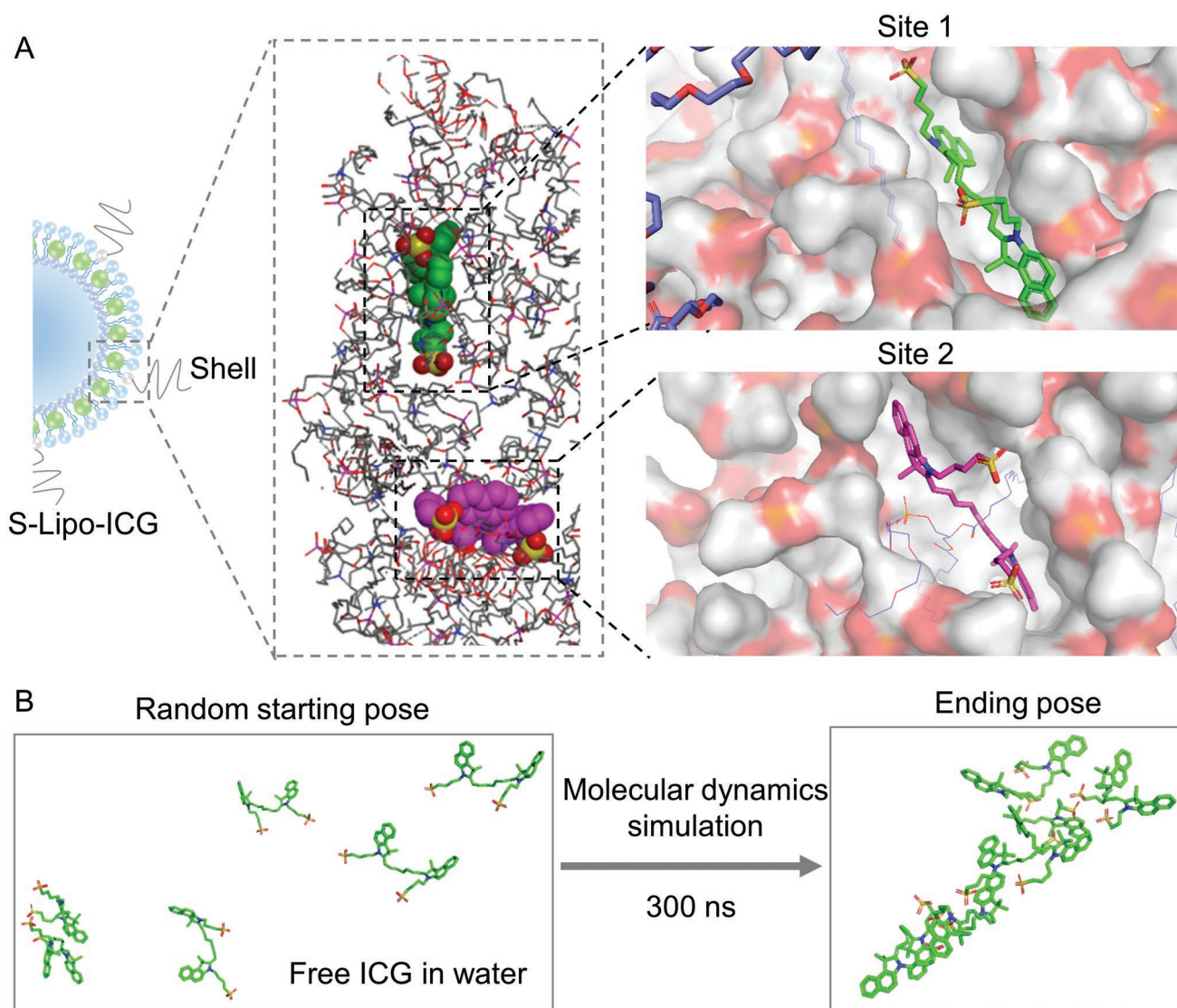
ADVANCED
SCIENCE NEWS
www.advancedsciencenews.com

NANO · MICRO
small
www.small-journal.com

Figure 3. The possible interaction mechanism between ICG and liposomes. A) Different binding modes of ICG and liposomes. (Green: site 1, purple: site 2, magnification zone: details of the binding positions of ICG and hydrophobic pockets of the liposome.) B) Molecular dynamics simulation the pose of free ICG in water.

time window is often longer than 30 min.[1d,16] Thus, multiple repeated i.v. injections of free ICG are required in the clinic to ensure imaging success, which may induce side effects. In our study, a single injection of S-Lipo-ICG is sufficient to meet imaging requirements. These findings demonstrate that, compared to free ICG, S-Lipo-ICG is a superior NIR-II fluorescent agent with greater brightness and a longer half-life in the blood.

2.5. Dual-Color Imaging

Multicolor fluorescence imaging can be used to simultaneously track several targets and visualize complex biological activities. This allows the identification of cancer subtypes, evaluation of immunotherapy outcomes, or guidance of

surgery.[17] Considering that S-Lipo-ICG and S-Lipo-FD1080 can be excited at 808 and 1064 nm, respectively, NIR-II dual-color imaging can be performed by adjusting the excitation wavelength (**Figure 5**A). The absorption spectra and NIR-II fluorescence emission spectra of free FD1080 and S-Lipo-FD1080, and cryo-electron microscopy images of S-Lipo-FD1080 were characterized for the further dual-color imaging (Figure S7, Supporting Information). To test our hypothesis, we examined the NIR-II fluorescence of S-Lipo-ICG and S-Lipo-FD1080 solutions under excitation at 808 and 1064 nm. As expected, the NIR-II fluorescence of S-Lipo-ICG solution could only be observed under 808 nm excitation, whereas the NIR-II fluorescence of the S-Lipo-FD1080 solution could be observed under 1064 nm excitation (Figure 5B). For comparison, free ICG (10 µg mL^{-1}) and FD1080 (30 µg mL^{-1}) are not bright sufficiently for dual-color imaging under the same

**ADVANCED
SCIENCE NEWS**

www.advancedsciencenews.com

NANO · MICRO

small
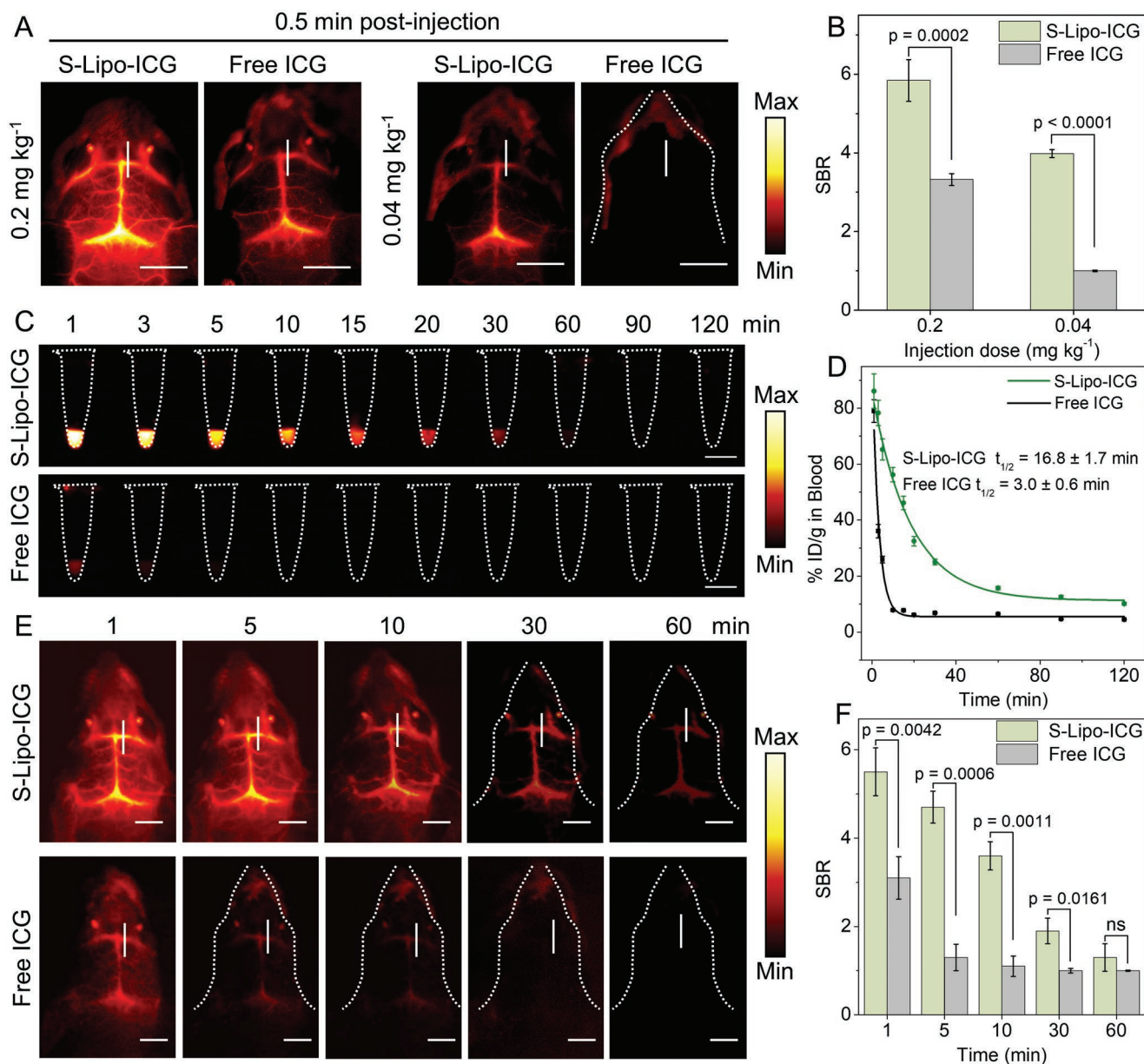
www.small-journal.com

Figure 4. High NIR-II fluorescence contrast and long circulation of S-Lipo-ICG. A) Cerebrovascular NIR-II fluorescence imaging in mice by i.v. injection of different doses of S-Lipo-ICG (ICG, 0.2, 0.04 mg kg^{-1}) and free ICG (0.2, 0.04 mg kg^{-1}) under 808 nm laser (0.1 W cm^{-2}, 1000 ms) irradiation using 1300 nm long-pass filters. B) The SBR of the region marked by a white line in (A). C) The blood samples collected from mice after i.v. injection of free ICG or S-Lipo-ICG at different time points. D) Blood circulation (%ID/g) of free ICG and S-Lipo-ICG administrated mice as a function of time. E) Cerebrovascular NIR-II fluorescence imaging in mice treated with free ICG (i.v. dose: 3 mg kg^{-1}) and S-Lipo-ICG (i.v. dose: 0.3 mg kg^{-1}) under laser irradiation (808 nm, 0.05 W cm^{-2}, 300 ms, LP1300). F) The SBR of the region marked by a white line in (E). Results are shown as the mean ± s.d. ($n = 5$), ns means no significant difference, two-tailed Student's t-test. Scale bars: 5 mm.

conditions in both aqueous solutions (Figure 5C) and blood (Figure S8, Supporting Information). Next, we employed S-Lipo-ICG (ICG, 5.2 nmol, i.v.) and S-Lipo-FD1080 (FD1080, 2.6 nmol, intradermal injection) to perform dual-color NIR-II imaging of the blood arteries and lymph nodes in mouse models. By switching the excitation wavelength at 10 min postinjection, vascular architecture, and lymph node could be distinguished (Figure 5D). Moreover, tumors and their angiogenesis could be detected by intratumoral injection of

S-Lipo-FD1080 and i.v. injection of S-Lipo-ICG, which could be beneficial for imaging-guided surgery for cancer therapy (Figure 5E). Unfortunately, previous multicolor lymphatic and circulatory imaging with cyanine dyes generally employed a tenfold higher dye dose (e.g., 323 nmol for ICG).[2c,8b,18] These results illustrate that our liposome-encapsulation approach not only enables in vivo multicolor NIR-II fluorescence imaging for cyanine dyes but also reduces the dye dose, which helps to reduce the costs and side effects.
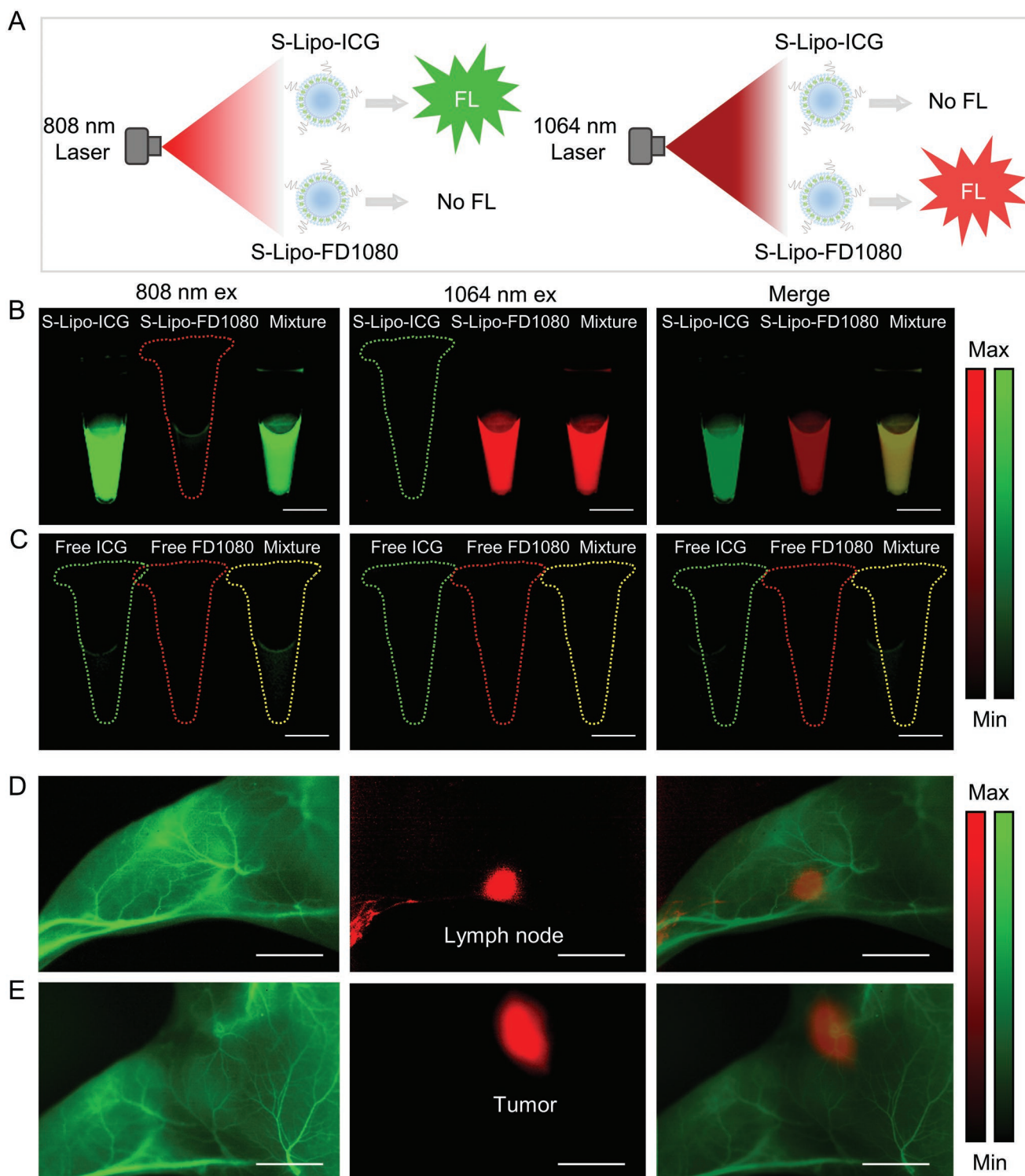
Figure 5. In vivo excitation-dependent dual-color NIR-II imaging. A) Scheme of the dual-color imaging of S-Lipo-ICG and S-Lipo-FD1080 distinguished by adjusting excitation wavelengths. B) Dual-color NIR-II imaging of S-Lipo-ICG, S-Lipo-FD1080, and mixed solutions under 808 and 1064 nm excitation, respectively. C) NIR-II fluorescence images of free ICG, free FD1080, and mixed solutions under 808 and 1064 nm laser excitation, respectively. D) In vivo dual-color NIR-II imaging of blood vessels and lymph node with i.v. injection of S-Lipo-ICG and intradermal injection of S-Lipo-FD1080. E) In vivo dual-color NIR-II imaging of blood vessels and tumor with i.v. injection of S-Lipo-ICG and intratumoral injection of S-Lipo-FD1080. Imaging conditions: 0.1 W cm^{-2}, 300 ms, LP1300. Scale bars: 5 mm.

2.6. In Vivo Tumor Imaging and Image-Guided Surgery in VX2 Tumor-Bearing Rabbit Models

In addition to the aforementioned advantages, the high-pressure homogenization-based encapsulation strategy can produce uniform liposome-encapsulated cyanine dyes on a large scale (Figure S9, Supporting Information), facilitating NIR-II imaging in large animals. To evaluate the feasibility, the produced S-Lipo-ICG (0.5 mg kg^{-1}) or free ICG (0.5 mg kg^{-1}) was administered into VX2 tumor-bearing rabbits through ear-vein injection (**Figure 6**A). The VX2 tumor was visualized at 0.5 h postinjection of S-Lipo-ICG, and the fluorescent signal of tumors lasted more than 8 h. In addition, the fluorescence signals around the tumor nearly disappeared 4 h after injection, leading to a clear tumor margin. By contrast, the tumor of the free ICG group could be monitored as early as 5 min after injection, and the fluorescence signals were no longer seen 10 min later. Quantitative analysis demonstrated that the SBR of the VX2 tumor was gradually increased in S-Lipo-ICG-treated rabbits and reached the maximum (SBR = 4.2) after 6 h (Figure 6B,C). However, the maximum SBR of the tumor in ICG-treated rabbits was only ≈1.6, which was ≈3-times lower than that of S-Lipo-ICG-treated

rabbits (Figure 6E). Then, the image-guided surgical removal of the VX2 tumor was conducted 6 h postinjection of S-Lipo-ICG, as this ensures a high SBR and a long imaging time window. Under the guidance of NIR-II fluorescence, tumor margins and small residual tumor tissues with a size of 2–5 mm can be distinguished from normal tissue. This can aid the successful removal of the tumor (Figure 6D). In addition, S-Lipo-ICG can also be utilized for deep-tissue NIR-II imaging, such as the liver and intestine of rabbits, because their depths are 7.2 and 4.2 mm, respectively, based on ultrasound imaging results (Figure S10, Supporting Information).

2.7. In Vivo Metabolism and Toxicity of S-Lipo-ICG

It is important to evaluate the metabolism and biocompatibility of S-Lipo-ICG for clinical translation. As an FDA-approved dye, ICG can be metabolized by the liver and excreted through feces in humans.[19] To explore the clearance path of S-Lipo-ICG, we measured its metabolism in healthy nude mice at various time points. As shown in **Figure 7**A, NIR-II fluorescence signals in the liver could be observed at 5 min i.v. postinjection
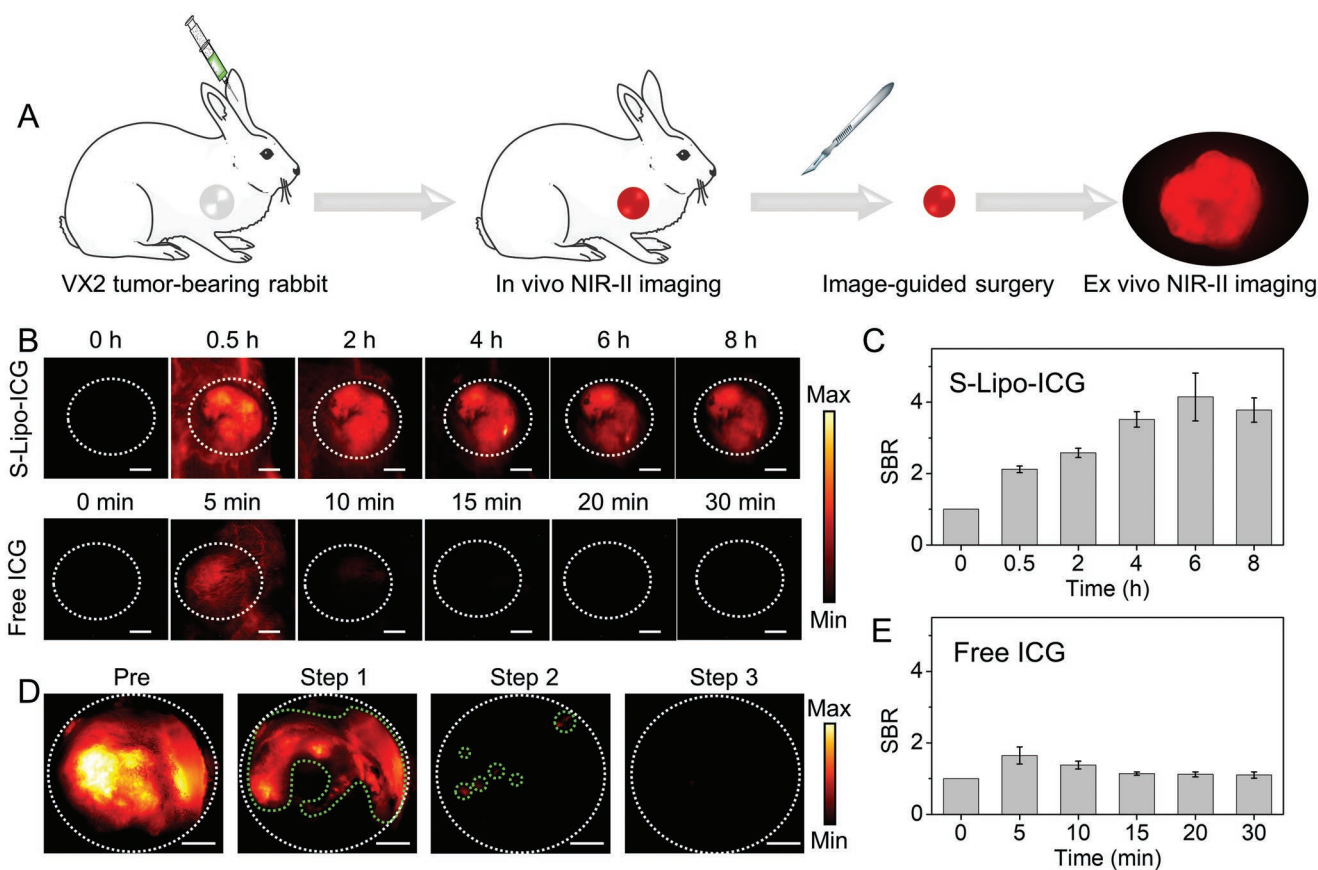

Figure 6. In vivo tumor imaging and image-guided surgery in VX2 tumor-bearing rabbit models. A) Schematic illustration of VX2 tumor image-guided surgery. B) NIR-II fluorescence images of VX2 tumor treated by S-Lipo-ICG and free ICG in rabbit models. C) Quantitative analysis of SBR of the VX2 tumor after ear-vein injection of S-Lipo-ICG. D) NIR-II fluorescence image-guided surgery after ear-vein injection of S-Lipo-ICG. E) Quantitative analysis of SBR of the VX2 tumor at different time points after administration of S-Lipo-ICG. The white circle indicates the tumor region and the green circle indicates the residual tumor area. (0.05 W cm^{-2}, 10 ms, LP1000). Scale bars: 1 cm. The green circles indicate residual tumor tissue. The data are presented as the mean ± s.d. (*n* = 3).
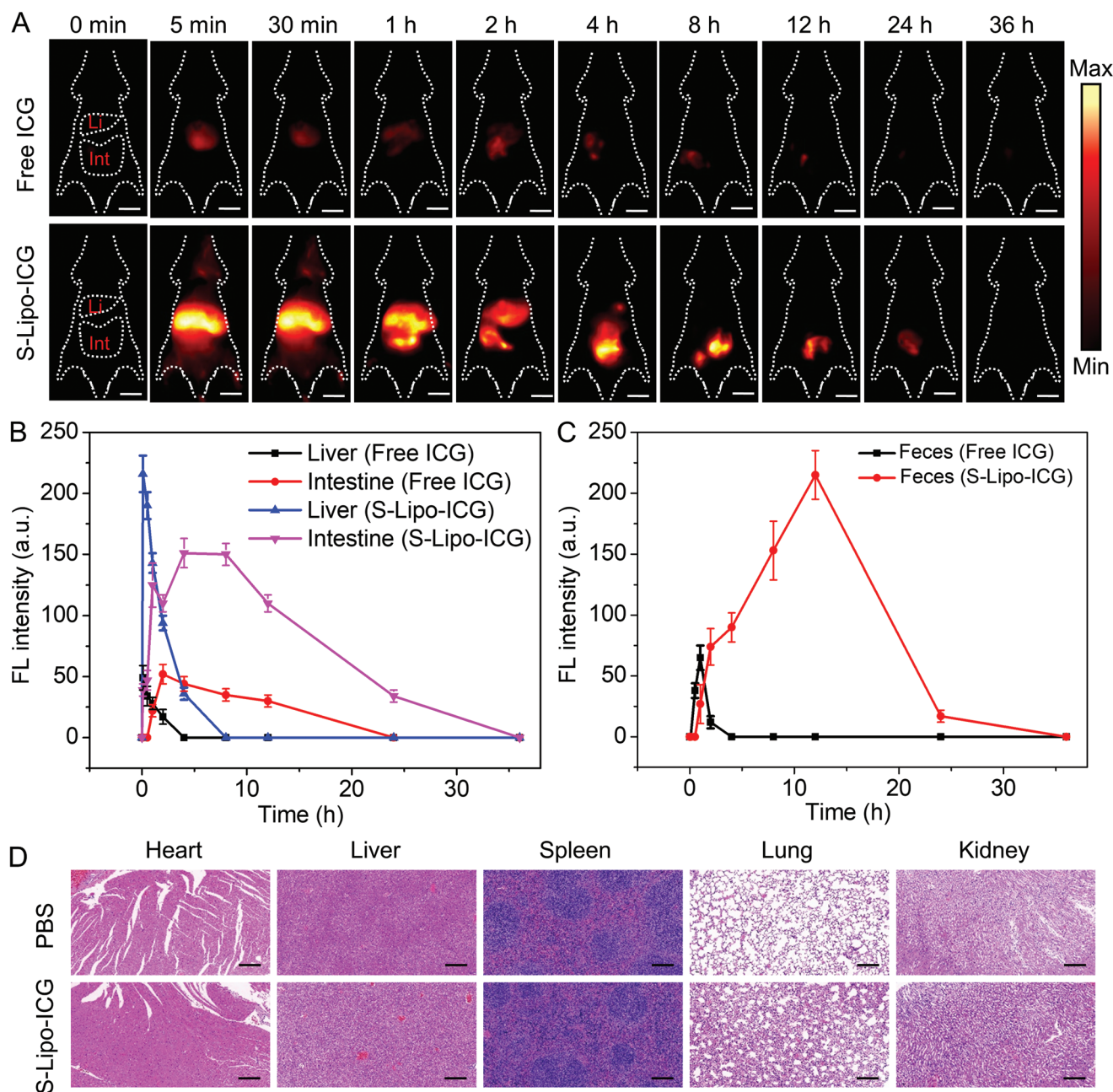
Figure 7. Metabolism of free ICG and S-Lipo-ICG in mice. A) NIR-II imaging of free ICG and S-Lipo-ICG in healthy nude mice (dose of ICG = 0.15 mg kg^{-1}, scale bars: 1 cm, Li indicates liver and Int indicates intestine, 0.05 W cm^{-2}, 5 ms, LP1000). B) Representative fluorescence signal intensity of liver and intestine regions for free ICG and S-Lipo-ICG at different time points. C) NIR-II fluorescence signals of feces excreted from mice treated with free ICG and S-Lipo-ICG, respectively. D) Representative H&E-stained images of major organs obtained from mice sacrificed 3 d after i.v. injection of PBS and S-Lipo-ICG. Scale bars: 200 µm. The data is presented as the mean ± s.d. ($n = 3$).

of free ICG and S-Lipo-ICG, and gradually declined until they were undetectable at 2 h and 4 h i.v. postinjection, respectively. Accordingly, NIR-II signals in the intestine increased with time, initially 2 h for free ICG and 8 h for S-Lipo-ICG, and finally disappeared after 24 and 36 h, respectively. This indicates that the S-Lipo-ICG-treated group had slower liver metabolism than free ICG. The prolongation of the metabolic duration may be attributed to the longer half-life time of S-Lipo-ICG in blood. Nevertheless, the trend of NIR-II fluorescence intensity fluctuation in the liver and intestine in the S-Lipo-ICG-treated group was consistent with that in the free ICG-treated group, indicating the same metabolic pathways (Figure 7B). The feces of the free ICG-treated and S-Lipo-ICG-treated mice showed strong NIR-II fluorescence (Figure 7C; Figure S11, Supporting Information). It further revealed that S-Lipo-ICG could be cleared from the body, consistent with free ICG. This indicates that the liposome-encapsulation strategy does not change the inherent metabolic process of ICG. Next, the in vivo toxicity of

**ADVANCED
SCIENCE NEWS**

www.advancedsciencenews.com

NANO · MICRO

small

www.small-journal.com

S-Lipo-ICG was evaluated using hematoxylin and eosin (H&E) staining. After administration of S-Lipo-ICG with a dose of 0, 0.5, 5, and 10 mg kg^{-1}, no apparent abnormalities or lesions of the organ slices were observed in the organ slices (Figure 7D; Figure S12, Supporting Information). The measurements of representative parameters of liver function and indicators of kidney function at the doses tested reveal no hepatic or kidney toxicity (Figure S13, Supporting Information).

3. Conclusion

We have developed a strategy for encapsulating cyanine dyes by high-pressure homogenization to construct liposome-cyanine dyes with enhanced NIR-II brightness. The results of computational modeling indicated a strong hydrophobic interaction between the liposomes and ICG, resulting in a stable complex. The brightness enhancement may be attributed to the bathochromic shift of the absorption peak and suppressed non-radiative transitions. Using S-Lipo-ICG as a representative dye for in vivo imaging, we found that S-Lipo-ICG exhibited improved NIR-II imaging performance and prolonged half-decay time, allowing higher SBR, lower ICG dosage, and longer imaging window compared with free ICG. Moreover, dual-color NIR-II fluorescence imaging of blood vessels and lymph nodes, as well as tumors and their angiogenesis was realized using S-Lipo-ICG and S-Lipo-FD1080, broadening the applications of free ICG and FD1080. S-Lipo-ICG was easily scaled up for large tumor (VX2 tumor) imaging and imaging-guided surgery in a rabbit model. Moreover, S-Lipo-ICG possesses similar metabolic pathways as free ICG and shows good biocompatibility. Most importantly, each component of S-Lipo-ICG, including ICG, DOPC, and DSPE-PEG$_{2000}$, is FDA-approved, facilitating clinical application. The simple ingredients and high-pressure homogenization method facilitate the synthesis of S-Lipo-ICG on a large scale and at a high quality, which can further promote clinical implementation.

4. Experimental Section

Materials: The DOPC and DSPE-PEG$_{2000}$ were obtained from Xi'an Ruixi Biological Technology Co., Ltd. ICG, and IR780 were purchased from Sigma-Aldrich. PBS was received from Hyclone. All commercial reagents were used as received without further purification. Ultrapure water was supplied for the needed experiments.

Synthesis of S-Lipo-Cyanine Dyes: Liposome-cyanine dyes were synthesized using a modified thin-film hydration method. Briefly, the lipid stock solution was prepared by dissolving DOPC and DSPE-PEG$_{2000}$ in CHCl$_3$ in a 19:1 molar ratio. ICG was dissolved in methanol at a concentration of 2 mg mL^{-1}. Subsequently, an adequate amount of ICG was mixed with the lipid at various molar ratios (Lipid/ICG), including 15.6:1, 31.3:1, 62.5:1, 125:1, 250:1, 500:1, and 750:1. The organic solvents were then removed using rotary evaporation to form a film layer, which was further dried in vacuo for 4 h. It was placed in PBS and hydrated in a water bath (65 °C, 10 min). The lipid-ICG PBS solution was freeze-thawed in a water bath (65 °C) and liquid nitrogen for 5 cycles and then subjected to high-pressure homogenization three times at 40 psi. The S-Lipo-ICG was further dialyzed to remove the free ICG molecules. S-Lipo-IR780 and S-Lipo-FD1080 were obtained by replacing ICG with IR780 and FD1080, respectively, using a similar method.

Cryo-Transmission Electron Microscope (Cryo-TEM): Lipid vesicles and S-Lipo-ICG (lipid, 6 mg mL^{-1}) were prepared and characterized by cryo-TEM. Five microliters of samples were dropped to 300-mesh copper grids with carbon films, which were blotted with filter paper after 4 s. The copper grids were immediately immersed in liquid ethane and stored under liquid nitrogen until they were transferred to the electron microscope for imaging. Images were acquired on a Krios G3i electron microscope (300 kV, Thermo Scientific) at a magnification of 59 000×.

Optical Properties of the S-Lipo-Cyanine Dyes: The absorption of cyanine dyes, including ICG, IR780, FD1080, and liposome-cyanine dyes was recorded using a PerkinElmer Lambda 750 UV–vis–NIR spectrophotometer. The emission of these solutions between 1000 and 1650 nm was recorded using 808 nm laser as the excitation source and a 1000-nm long-pass filter as the emission filter by F900 fluorescence spectrophotometer (Edinburgh Instruments, Ltd., U.K). The fluorescence intensity of free ICG and S-Lipo-ICG was detected every 3 days under ambient conditions for ≈15 days. Also, the diameter of S-Lipo-ICG was recorded every 3 days by dynamic light scattering.

Measurements of NIR-II QYs: The quantum yield increments in the NIR-II window of S-Lipo-cyanine dyes were measured using free dyes (ICG, IR780, and FD1080) as references. Taking ICG as an example, ICG solution with five different absorption values below 0.1 at 808 nm was prepared. The emission of these solutions between 1000 and 1650 nm was recorded using an 808 nm laser as the excitation source and a 1000-nm long-pass filter as the emission filter. The integrated NIR-II area as a function of the absorption value at 808 nm was then determined. The slope of S-Lipo-ICG was also obtained using the same method. The quantum yield increment (Slope$_{S-Lipo-ICG}$/Slope$_{ICG}$) of S-Lipo-ICG was further determined. Similarly, the QY increment of S-Lipo-IR780 was determined. For FD1080, the excitation and the absorption values were changed from 808 to 1064 nm. The QY increment (Slope$_{S-Lipo-FD1080}$/Slope$_{FD1080}$) of S-Lipo-FD1080 was measured using the same procedure.

Computational Modeling: Molecular coordinates of the dyes were downloaded from Pubchem (https://pubchem.ncbi.nlm.nih.gov/), and the bilayer lipid membrane system was constructed by CHARM-GUI (https://charmm-gui.org/), with 95 DOPC and 5 DSPE-PEG$_{2000}$ in each monolayer. The initial binding position of ICG in the membrane was calculated. The cavities of the liposome were centered on the origin, and the 60 × 60 × 60 Å grid box was set as the search space for the best conformations of ICG. Molecular docking simulations were further conducted. The Lamarckian genetic algorithm was used with a population size of 150 individuals, whereas 250 000 energy evaluations were used for 100 times repetition to obtain the optimal pose. The conformations with the lowest binding energies were selected for further analysis. Four ICGs docked at different sites in the membrane system were used for the molecular dynamics (MD) investigation. The system was further minimized and equilibrium by NVT, and submitted for 300 ns MD under the Charmm force field using GROMACS. The main conformation of ICG in the membrane was further analyzed by Gaussian.

Pharmacokinetic Studies: Animal procedures were performed with the approval of the Animal Care and Use Committee of Shenzhen Institutes of Advanced Technology, Chinese Academic of Sciences. Six-week-old female Balb/c mice with three mice per group were adopted for pharmacokinetics study. S-Lipo-ICG or ICG saline was intravenously (i.v.) injected into the mice via the tail vein at a dose of 0.5 mg kg^{-1}. 2 μL of blood was collected from the tail at different time points. The concentration of S-Lipo-ICG and free ICG in blood was calculated by the NIR-II fluorescence imaging system (808 nm, long pass 1000 nm). The percent injected dose per gram (%ID/g) of blood was calculated using the following equation

$$\%ID/g = \frac{C_{\text{sample in blood}} \times V_{\text{blood}}}{C_{\text{injected sample}} \times V_{\text{injected}} \times \text{blood weight}} \times 100\% \tag{1}$$

In Vivo NIR-II Fluorescence Imaging: To compare the in vivo NIR-II imaging performance of the free ICG and S-Lipo-ICG, free ICG (dose: 0.2, 0.04, and 3 mg kg^{-1}) and S-Lipo-ICG (dose: 0.2, 0.04, and 0.3 mg kg^{-1}) were administered to healthy C57BL/6J mice via tail-vein injection. The cerebrovascular fluorescence images of the mice were further

ADVANCED
SCIENCE NEWS
www.advancedsciencenews.com

NANO · MICRO
small
www.small-journal.com

recorded at various time points using the NIR-II fluorescence imaging system (NIRvana 640, Teledyne Princeton Instruments; 808 nm, long pass 1300 nm).

For the dual-color imaging of blood vessels and lymph nodes/tumors, S-Lipo-ICG (i.v. injection) and S-Lipo-FD1080 (intradermal/intratumor injection) were excited by exposure to an 808 nm laser and a 1064 nm laser, respectively. The fluorescence signal was recorded by the camera with a 1300 nm long-pass filter. The dual-color fluorescence images were merged in ImageJ software.

To show the NIR-II imaging ability of the probes, a long-pass filter of 1000 nm at 808 nm laser excitation and a long-pass filter of 1100 nm at 1064 nm laser excitation were chosen in the experiments. To show the high spatial resolution such as cerebrovascular and other vessels, a long-pass filter of 1300 nm was used in the experiments.

Image-Guided Surgery in VX2 Tumor-Bearing Rabbit Models: VX2 tumor-bearing rabbits were received from Guangdong Medical Laboratory Animal Center. The NIR-II fluorescence images of the tumor were acquired at different instances after the ear-vein injection of the S-Lipo-ICG (0.5 mg kg^{-1}) or free ICG (0.5 mg kg^{-1}) using the NIR-II fluorescence imaging system (808 nm, long pass 1000 nm). The image-guided surgical removal of the VX2 tumor was carried out at 6 h after S-Lipo-ICG administration, and the removed tumor was further imaged using the NIR-II fluorescence imaging system.

In Vivo Toxicity Evaluation of the S-Lipo-ICG: S-Lipo-ICG at doses 0.5, 5, and 10 mg kg^{-1} was administrated into mice by i.v. injection. Blood samples were collected at 1-, 2-, and 3 days postinjection. PBS-treated mice were used as the control group. The blood and biochemical indexes of the mice were further measured in Shanghai Biomodel Organism. Major organs were also collected from mice injected with S-Lipo-ICG and PBS. After treatment of the tissues with 4% formalin, H&E staining was carried out and the tissues were embedded in paraffin. Images were further recorded using a digital microscope (Nikon Eclipse 90i).

Statistical Analysis: Quantitative results are expressed as mean ± s.d. Two-tailed Student's *t*-test was used for statistical analysis of two groups ($n = 5$). Significant differences are indicated by P values of less than 0.05. The results were analyzed with Microsoft Excel software.

Supporting Information

Supporting Information is available from the Wiley Online Library or from the author.

Conflict of Interest

The authors declare no conflict of interest.

Data Availability Statement

The data that support the findings of this study are available from the corresponding author upon reasonable request.

[1] a) S. He, J. Song, J. Qu, Z. Cheng, *Chem. Soc. Rev.* **2018**, *47*, 4258; b) A. M. Smith, M. C. Mancini, S. Nie, *Nat. Nanotechnol.* **2009**, *4*, 710; c) G. Hong, A. L. Antaris, H. Dai, *Nat. Biomed. Eng.* **2017**, *1*, 0010; d) Z. Hu, C. Fang, B. Li, Z. Zhang, C. Cao, M. Cai, S. Su, X. Sun, X. Shi, C. Li, T. Zhou, Y. Zhang, C. Chi, P. He, X. Xia, Y. Chen, S. S. Gambhir, Z. Cheng, J. Tian, *Nat. Biomed. Eng.* **2020**, *4*, 259.

[2] a) H. Wan, H. Du, F. Wang, H. Dai, *Adv. Funct. Mater.* **2019**, *29*, 1900566; b) J. Huang, C. Xie, X. Zhang, Y. Jiang, J. Li, Q. Fan, K. Pu, *Angew. Chem., Int. Ed.* **2019**, *58*, 15120; c) O. T. Bruns, T. S. Bischof, D. K. Harris, D. Franke, Y. Shi, L. Riedemann, A. Bartelt, F. B. Jaworski, J. A. Carr, C. J. Rowlands, M. W. B. Wilson, O. Chen, H. Wei, G. W. Hwang, D. M. Montana, I. Coropceanu, O. B. Achorn, J. Kloepper, J. Heeren, P. T. C. So, D. Fukumura, K. F. Jensen, R. K. Jain, M. G. Bawendi, *Nat. Biomed. Eng.* **2017**, *1*, 0056.

[3] a) X.-D. Zhang, H. Wang, A. L. Antaris, L. Li, S. Diao, R. Ma, A. Nguyen, G. Hong, Z. Ma, J. Wang, S. Zhu, J. M. Castellano, T. Wyss-Coray, Y. Liang, J. Luo, H. Dai, *Adv. Mater.* **2016**, *28*, 6872; b) H. Wan, J. Yue, S. Zhu, T. Uno, X. Zhang, Q. Yang, K. Yu, G. Hong, J. Wang, L. Li, Z. Ma, H. Gao, Y. Zhong, J. Su, A. L. Antaris, Y. Xia, J. Luo, Y. Liang, H. Dai, *Nat. Commun.* **2018**, *9*, 1171; c) D. Gao, Y. Li, Y. Wu, L. Liu, D. Hu, S. Liang, J. Liao, M. Pan, P. Zhang, K. Li, X. Liu, H. Zheng, Z. Sheng, *ACS Appl. Mater. Interfaces* **2022**, *15*, 3; d) A. L. Antaris, H. Chen, K. Cheng, Y. Sun, G. Hong, C. Qu, S. Diao, Z. Deng, X. Hu, B. Zhang, X. Zhang, O. K. Yaghi, Z. R. Alamparambil, X. Hong, Z. Cheng, H. Dai, *Nat. Mater.* **2016**, *15*, 235.

[4] a) Y. Ji, C. Jones, Y. Baek, G. K. Park, S. Kashiwagi, H. S. Choi, *Adv. Drug Delivery Rev.* **2020**, *167*, 121; b) N. Liao, L. Su, Y. Zheng, B. Zhao, M. Wu, D. Zhang, H. Yang, X. Liu, J. Song, *Angew. Chem., Int. Ed.* **2021**, *60*, 20888; c) G.-T. Yu, M.-Y. Luo, H. Li, S. Chen, B. Huang, Z.-J. Sun, R. Cui, M. Zhang, *ACS Nano* **2019**, *13*, 12830; d) Y. Zhong, Z. Ma, F. Wang, X. Wang, Y. Yang, Y. Liu, X. Zhao, J. Li, H. Du, M. Zhang, Q. Cui, S. Zhu, Q. Sun, H. Wan, Y. Tian, Q. Liu, W. Wang, K. C. Garcia, H. Dai, *Nat. Biotechnol.* **2019**, *37*, 1322.

[5] a) H. Liu, G. Hong, Z. Luo, J. Chen, J. Chang, M. Gong, H. He, J. Yang, X. Yuan, L. Li, X. Mu, J. Wang, W. Mi, J. Luo, J. Xie, X.-D. Zhang, *Adv. Mater.* **2019**, *31*, 1901015; b) B. Li, M. Zhao, L. Feng, C. Dou, S. Ding, G. Zhou, L. Lu, H. Zhang, F. Chen, X. Li, G. Li, S. Zhao, C. Jiang, Y. Wang, D. Zhao, Y. Cheng, F. Zhang, *Nat. Commun.* **2020**, *11*, 3102; c) M. Zhang, J. Yue, R. Cui, Z. Ma, H. Wan, F. Wang, S. Zhu, Y. Zhou, Y. Kuang, Y. Zhong, D.-W. Pang, H. Dai, *Proc. Natl. Acad. Sci. USA* **2018**, *115*, 6590.

[6] a) M. Zhao, R. Wang, B. Li, Y. Fan, Y. Wu, X. Zhu, F. Zhang, *Angew. Chem., Int. Ed. Engl.* **2019**, *58*, 2050; b) P. Wang, Y. Fan, L. Lu, L. Liu, L. Fan, M. Zhao, Y. Xie, C. Xu, F. Zhang, *Nat. Commun.* **2018**, *9*, 2898; c) C. Yao, Y. Chen, M. Zhao, S. Wang, B. Wu, Y. Yang, D. Yin, P. Yu, H. Zhang, F. Zhang, *Angew. Chem., Int. Ed.* **2022**, *61*, 202114273.

[7] a) G. Hong, S. Diao, J. Chang, A. L. Antaris, C. Chen, B. Zhang, S. Zhao, D. N. Atochin, P. L. Huang, K. I. Andreasson, C. J. Kuo, H. Dai, *Nat. Photonics* **2014**, *8*, 723; b) J. Li, Y. Liu, Y. Xu, L. Li, Y. Sun, W. Huang, *Coord. Chem. Rev.* **2020**, *415*, 213318; c) P. Pei,

**ADVANCED
SCIENCE NEWS**

www.advancedsciencenews.com

**NANO · MICRO
small**

www.small-journal.com

Y. Chen, C. Sun, Y. Fan, Y. Yang, X. Liu, L. Lu, M. Zhao, H. Zhang, D. Zhao, X. Liu, F. Zhang, *Nat. Nanotechnol.* **2021**, *16*, 1011; d) H. Ma, J. Wang, X.-D. Zhang, *Coord. Chem. Rev.* **2021**, *448*, 214184; e) Y. Liu, Y. Li, S. Koo, Y. Sun, Y. Liu, X. Liu, Y. Pan, Z. Zhang, M. Du, S. Lu, X. Qiao, J. Gao, X. Wang, Z. Deng, X. Meng, Y. Xiao, J. S. Kim, X. Hong, *Chem. Rev.* **2022**, *122*, 209; f) J. Mei, N. L. C. Leung, R. T. K. Kwok, J. W. Y. Lam, B. Z. Tang, *Chem. Rev.* **2015**, *115*, 11718.

[8] a) H. Kang, M. Shamim, X. Yin, E. Adluru, T. Fukuda, S. Yokomizo, H. Chang, S. H. Park, Y. Cui, A. J. Moy, S. Kashiwagi, M. Henary, H. S. Choi, *Adv. Mater.* **2022**, *34*, 2106500; b) E. D. Cosco, A. L. Spearman, S. Ramakrishnan, J. G. Lingg, M. Saccomano, M. Pengshung, B. A. Arús, K. C. Wong, S. Glasl, V. Ntziachristos, *Nat. Chem.* **2020**, *12*, 1123; c) D. S. Keller, T. Ishizawa, R. Cohen, M. Chand, *Lancet Gastroenterol. Hepatol.* **2017**, *2*, 757; d) R. Ma, X. Tang, M. Wang, Z. Du, S. Chen, Y. Heng, L. Zhu, N. Alifu, X. Zhang, C. Ma, *Nanomedicine* **2023**, *47*, 102615; e) R. Bhavane, Z. Starosolski, I. Stupin, K. Ghaghada, A. Annapragada, *Sci. Rep.* **2018**, *8*, 14455.

[9] a) R. Tian, Q. Zeng, S. Zhu, J. Lau, S. Chandra, R. Ertsey, K. S. Hettie, T. Teraphongphom, Z. Hu, G. Niu, *Sci. Adv.* **2019**, *5*, 0672; b) C. Sun, B. Li, M. Zhao, S. Wang, Z. Lei, L. Lu, H. Zhang, L. Feng, C. Dou, D. Yin, H. Xu, Y. Cheng, F. Zhang, *J. Am. Chem. Soc.* **2019**, *141*, 19221; c) J. C. Kraft, R. J. Y. Ho, *Biochemistry* **2014**, *53*, 1275; d) Y. Jia, X. Wang, D. Hu, P. Wang, Q. Liu, X. Zhang, J. Jiang, X. Liu, Z. Sheng, B. Liu, H. Zheng, *ACS Nano* **2019**, *13*, 386; e) S. Zhu, Z. Hu, R. Tian, B. C. Yung, Q. Yang, S. Zhao, D. O. Kiesewetter, G. Niu, H. Sun, A. L. Antaris, X. Chen, *Adv. Mater.* **2018**, *30*, 1802546; f) G. Yeroslavsky, M. Umezawa, K. Okubo, K. Nigoghossian, D. T. Kim Dung, K. Miyata, M. Kamimura, K. Soga, *Biomater. Sci.* **2020**, *8*, 2245.

[10] P. Vinchhi, J. K. Patel, M. M. Patel, *Emerging Technologies for Nanoparticle Manufacturing*, Springer, Cham **2021**, Ch. 11.

[11] B. Li, L. Lu, M. Zhao, Z. Lei, F. Zhang, *Angew. Chem., Int. Ed.* **2018**, *57*, 7483.

[12] Z. Sheng, Y. Li, D. Hu, T. Min, D. Gao, J. S. Ni, P. Zhang, Y. Wang, X. Liu, K. Li, H. Zheng, B. Z. Tang, *Research* **2020**, *2020*, 4074593.

[13] B. Guo, Z. Feng, D. Hu, S. Xu, E. Middha, Y. Pan, C. Liu, H. Zheng, J. Qian, Z. Sheng, B. Liu, *Adv. Mater.* **2019**, *31*, 1902504.

[14] H. Wan, H. Ma, S. Zhu, F. Wang, Y. Tian, R. Ma, Q. Yang, Z. Hu, T. Zhu, W. Wang, Z. Ma, M. Zhang, Y. Zhong, H. Sun, Y. Liang, H. Dai, *Adv. Funct. Mater.* **2018**, *28*, 1804956.

[15] H. Wang, X. Li, B. W. Tse, H. Yang, C. A. Thorling, Y. Liu, M. Touraud, J. B. Chouane, X. Liu, M. S. Roberts, X. Liang, *Theranostics* **2018**, *8*, 1227.

[16] E. H. Kim, J. M. Cho, J. H. Chang, S. H. Kim, K. S. Lee, *Acta Neurochir.* **2011**, *153*, 1487.

[17] a) R. Tian, H. Ma, S. Zhu, J. Lau, R. Ma, Y. Liu, L. Lin, S. Chandra, S. Wang, X. Zhu, H. Deng, G. Niu, M. Zhang, A. L. Antaris, K. S. Hettie, B. Yang, Y. Liang, X. Chen, *Adv. Mater.* **2020**, *32*, 1907365; b) Y. Fan, P. Wang, Y. Lu, R. Wang, L. Zhou, X. Zheng, X. Li, J. A. Piper, F. Zhang, *Nat. Nanotechnol.* **2018**, *13*, 941; c) Z. Lei, C. Sun, P. Pei, S. Wang, D. Li, X. Zhang, F. Zhang, *Angew. Chem., Int. Ed.* **2019**, *58*, 8166.

[18] E. D. Cosco, B. A. Arús, A. L. Spearman, T. L. Atallah, I. Lim, O. S. Leland, J. R. Caram, T. S. Bischof, O. T. Bruns, E. M. Sletten, *J. Am. Chem. Soc.* **2021**, *143*, 6836.

[19] T. Ishizawa, N. Fukushima, J. Shibahara, K. Masuda, S. Tamura, T. Aoki, K. Hasegawa, Y. Beck, M. Fukayama, N. Kokudo, *Cancer* **2009**, *115*, 2491.